Available online at www.sciencedirect.com

SciVerse ScienceDirect

Ceramics International 39 (2013) 2955–2966

CERAMICS INTERNATIONAL

www.elsevier.com/locate/ceramint

Crystallisation and microstructure of nepheline–forsterite glass-ceramics

M.I. Martín[a], F. Andreola[b], L. Barbieri[b], F. Bondioli[b], I. Lancellotti[b], J.Ma. Rincón[a], M. Romero[a,*]

[a]Group of Glassy and Ceramic Materials, Department of Construction, Eduardo Torroja Institute for Construction Science (IETcc), CSIC, Serrano Galvache 4, 28033 Madrid, Spain

[b]Dipartimento di Ingegneria dei Materiali e dell'Ambiente, Università degli Studi di Modena e Reggio Emilia, Via Vignolese 905, 41125 Modena, Italy

Received 31 July 2012; received in revised form 21 September 2012; accepted 22 September 2012
Available online 11 October 2012

Abstract

This work presents the results of a study focused on the development of forsterite–nepheline glass-ceramic with the use of rice husk ash (RHA) as a silica source. The glass-ceramics were produced by a sintering process of a glassy frit formulated in the $MgO–Al_2O_3–SiO_2$ base system with the addition of B_2O_3 and Na_2O to facilitate the melting and pouring processes. The crystallisation study was carried out by depicting the TTT curve (Time–Temperature–Transformation). The mineralogical characterisation of the glass-ceramic materials was carried out using the X-ray diffraction (XRD). The crystallisation activation energies were calculated by the Kissinger method. The results obtained show that devitrification of the RHA glass leads to a glass-ceramic material composed of nepheline ($Na_2O \cdot Al_2O_3 \cdot 2SiO_2$) and forsterite ($2MgO \cdot SiO_2$). A study of the microstructure by scanning electron microscopy (SEM) allowed to establish the morphological evolution in both the shape and spatial arrangement of the nepheline and forsterite crystals on heating.

Keywords: A. Sintering; B. Microstructure-final; D. Glass-ceramics

1. Introduction

Glass-ceramics are established materials that exhibit advantageous thermal, optical, chemical, mechanical and electrical properties [1]. The great variety of compositions and the potential for the development of special microstructures with specific technological properties have allowed glass-ceramic materials to be used in a wide range of applications, such as kitchen cooktops [2], prostheses for surgical implants [3], glazes for ceramic tiles [4], telescope mirrors, radomes [5], insulators [1] and electronic packaging [6]. Glass-ceramics are produced from a parent glass by a sequential thermal process that involves controlled crystallisation, which consists of the growth of one or more crystalline phases within the vitreous mass [7]. The earliest glass-ceramics were produced by a conventional glass route and subsequently crystallised, usually by heat treatment in two stages to produce nucleation, which was followed by crystal growth. In recent years, the sintering method has proven to be a technically viable route for the manufacture of glass-ceramics. This process usually involves milling a glass frit into fine particles, which are then shaped by conventional forming techniques and subsequently heat treated to provide sintering and crystallisation of the glass particles. A sintering process is normally used when the parent glass exhibits a strong tendency for surface crystallisation or when complex shapes are required [8]. Because the most important forming systems are based on silicate compositions, the key crystalline phases of glass-ceramics are principally silicates [1].

Forsterite (Mg_2SiO_4) is the magnesium rich end-member of the olivine solid solution series [9], and it is endowed with low electrical conductivity and a low dielectric constant, refractoriness and excellent insulation properties (even at high temperatures) and good biocompatibility. All of these favourable technological properties have led to the adoption of forsterite in many important technologies,

*Corresponding author. Tel.: +34 91 302 04 40; fax: +34 91 302 07 00.
E-mail address: mromero@ietcc.csic.es (M. Romero).

0272-8842/$ - see front matter © 2012 Elsevier Ltd and Techna Group S.r.l. All rights reserved.
http://dx.doi.org/10.1016/j.ceramint.2012.09.072

including substrates for high-frequency electronics, ceramic-metal seals, the iron and steel industry, tunable lasers [10] and even as a bone implant material [11].

Forsterite has been synthesised by various techniques, including the conventional solid-state reaction of periclase (MgO) and silica (SiO_2) [12], the mechanical activation of a talc and magnesium carbonate powder mixture [13], the polymer precursor method [14] and the sol–gel method [15]. However, the sintering temperature of forsterite is approximately 1500 °C, which is too high and limits its use. Many efforts have been made to improve the workability of forsterite, including reduction of the firing temperature by the addition of alumina [16] or low melting point glasses [17]. Another possible way to produce forsterite materials at lower temperatures is through the glass-ceramic process. Indeed, several investigations report the devitrification of forsterite as a secondary crystalline phase in glass-ceramics belonging to different composition systems [18–22].

Nepheline ($NaAlSiO_4$) is a tectosilicate belonging to the also designated nepheline group $(Na,K)AlSiO_4$. The nepheline phase is characterised by high chemical mechanical strength and impact resistance. Nepheline-based glass-ceramics are demonstrated to be suitable for use in microwave ovens [23] and dental applications [24,25]. Nepheline glass-ceramics are usually prepared from glasses of the Na_2O–Al_2O_3–SiO_2 system and by the addition of different nucleating agents, such as TiO_2, Cr_2O_3, ZrO_2 or LiF to promote crystallisation [26,27].

Nepheline- and forsterite-containing glass-ceramics are normally prepared from high purity proportions of pure chemicals. They can also be prepared from cheaper raw materials such as wastes because the glass-ceramic process has been established as a suitable way to valorise mining and industrial wastes [5,28], including fly ash from incineration [29,30] and thermal power plants [4,31], wastes from hydrometallurgical processing plants [28], residual glass fibres from polyester matrix composites [32] and bagasse ashes [8], among others wastes. One residue that has experienced a significant increase in production in recent years is biomass ash, which originates from the combustion of biological material for energy purposes. It is clear that the current energy model in which more than 80% of energy production is based on fossil fuel consumption is not sustainable. For this reason, governments worldwide are implementing policies aimed at increasing the use of renewable energy resources. The use of biomass for energy purposes has multiple environmental benefits (i.e., reduction of CO_2 emissions, non-production of solid particles and sulphur and nitrogen pollutants, stimulation of economic growth in rural areas, reduction of dependence on external fuel supplies, and re-use of wastes generated by agricultural activities).

Rice husk ash (RHA) is a waste material that is produced by burning rice husks; in particular, it is produced when rice husks are used as fuel for kilns to produce bricks and other clay products or in rice mills to generate steam for the parboiling process. Rice husks contain approximately 75% organic volatile matter and the balance of 25% of the weight is converted into ash during the firing process. This ash, which is known as RHA, is a carbon neutral green product that contains approximately 85–90 (wt%) amorphous silica. Worldwide, approximately 120 Mt of rice husk are produced annually, which gives rise to a global production of 21 Mt/year of RHA [33]. In general, RHA is dumped as a waste [34,35]; however, because of its composition, it may be used as a source of silica in the steel industry [36] and as a pozzolanic material for the cement industry [37,38]. In the ceramic sector, several studies have been conducted in recent years to valorise RHA. In particular, the use of this ash has been investigated as a secondary raw material in the manufacture of whiteware products [39], pigments [34,40], glazes [35,41], brick compositions [42] and glass-ceramic materials in the SiO_2–Na_2O–CaO [43] and SiO_2–Al_2O_3–Li_2O [44] systems, as well as in cordierite-based glass-ceramics [45].

In a recent paper [33], the authors have demonstrated the feasibility of producing forsterite–nepheline-based glasses from a RHA mixture that incorporates B_2O_3 and Na_2O to facilitate the melting process. Significant environmental benefits are attained by using RHA as a source of silica: (a) avoided landfill disposal of the residue; (b) minimisation of the natural raw materials consumption. Besides, the RHA is a not hazardous residue, so the materials resulted do not cause further damage (environmental impact). These glasses could lead to glass-ceramics that combine the beneficial properties associated with both the forsterite (low electrical conductivity, low dielectric constant, refractoriness and excellent insulation properties) and nepheline (high mechanical strength and impact resistance) crystalline phases. The development of a material that combines these properties could find many applications, such as building material (ceramic tiles) in which these properties are required. It is known that the nature of the devitrified crystalline phases, as well as their shape, size and spatial arrangement, are the most important factors that affect the technical properties of glass-ceramics. Therefore, the aim of this work is to study the evolution of the crystalline phases and microstructures during the crystallisation process of a forsterite–nepheline-based glass produced from RHA as a silica source.

2. Materials and methods

A glass (hereafter designated RHA glass) in the SiO_2–Al_2O_3–MgO–Na_2O base system was formulated with rice husk ash from a plant producing semi-parboiled rice as a silica source (Garibaldi 1889, Colussi S.p.A., Milan, Italy). Prior to its use, the ash was sieved to a particle size < 250 μm. B_2O_3 and Na_2O (as Na_2CO_3) were added to the ash to facilitate the melting process. The chemical reagents used (all of A.R. quality) were Al_2O_3, MgO, B_2O_3 and Na_2CO_3. The components (46.52% ash, 13.84% Al_2O_3, 13.16% MgO, 22.17% Na_2CO_3 and 4.33% B_2O_3) were mixed for 30 min in a blender (TURBULA) to produce a

homogeneous mixture. The batch was placed in an aluminosilicate crucible and heated at 10 °C/min in an electric furnace up to 1450 °C. After a holding time of 120 min at the melting temperature, the melt was quenched by pouring into water, producing a glass frit.

The chemical compositions of the RHA and glass frit were determined by X-ray fluorescence (XRF) (Thermo Scientific model ARL ADVANT'XP) and inductively coupled plasma (ICP) (Varian model Liberty 200), respectively.

The activation energy for crystallisation was calculated by differential scanning calorimetry (DSC) (SETARAM model Labsys) on powder samples (< 63 μm). The samples were heated from 25 to 1450 °C at heating rates of 10°, 20°, 30°, 40° and 50 °C/min. The DSC scans were conducted under flowing air, in platinum crucibles and calcined Al_2O_3 was used as a reference material. The DSC curves were normalised with respect to the sample weight. The data were analysed using the Kissinger method [46]:

$$\ln\left(\beta/T_p^2\right) = -E/\mathrm{R}T_\mathrm{p} + \text{constant} \quad (1)$$

where T_p is the maximum of the DSC crystallisation peak, β is the heating rate, E is the activation energy and R is the ideal gas constant.

The development of the crystalline phases after heating of the final glass-ceramics was studied on compacted glass samples. Powdered glass (< 63 μm) was moistened by spraying with distilled water (2 wt%). Compacts (1×1 cm) were shaped by uniaxial pressing (Nannetti S hydraulic press) at 40 MPa in a steel die. The glass compacts were thermally treated at different temperatures (650–1000 °C) for several times (2–60 min). After treatment, the samples were taken out of the oven and cooled to room temperature.

The evaluation of the amorphous nature of the glass after melting and the mineralogical study of the crystalline phases devitrified after the thermal treatment was performed by X-ray diffraction (XRD) (Philips model X 'PERT MPD) with Ni-filtered Cu Kα radiation operating at 30 mA and 50 kV. Data were recorded in the 3–75° 2θ range (step size 0.019732° and 0.5 s counting time for each step).

The microstructural analysis of the glass-ceramic materials was performed by field emission scanning electron microscopy (FESEM) (JEOL model JSM 6500F) using an accelerating voltage of 20 kV. The SEM specimens were polished using 6, 3 and 1 μm diamond pastes after grinding with silicon carbide paper and water. The polished surfaces were etched for 10 s in a 5 vol% HF solution, washed ultrasonically with distilled water and ethyl alcohol, dried and subsequently Au–Pd coated in a Balzers SCD 050 sputter. Semi-quantitative analysis of the different phases was performed by energy dispersive X-ray spectroscopy (EDS) with a Link eXL detector provided by a beryllium (Be) window. The distribution of the Na and Mg ions among the different crystalline phases was determined by means of digital X-ray mapping, which is an imaging technique that is used to examine the two-dimensional distribution of elements in a specimen. Each two-dimensional map represents a single element and the colour variations on the map represent differences in the weight per cent of the elements from point to point.

To a first evaluation of the technological properties, the glass-ceramic crystallised for 40 min 900 °C were tested to determine the water absorption (ASTM C373-88), Mohs hardness using a laboratory kit (Gabbrielli Technology srl) and bending strength (UNI-EN 843-1) in an electronic universal tester (Servosis model ME-402/01) on ten test pieces of $50 \times 10 \times 3$ mm by a three point loading test with a span of 32 mm and a crosshead speed of 1 mm/min.

3. Results and discussion

Table 1 shows the chemical composition of the rice husk ash and the derived RHA glass. The major component of the ash SiO_2, and P_2O_5 shows the highest concentration among the minor components. SiO_2, Al_2O_3, Na_2O and MgO are the main components of the RHA glass. When the glass composition is represented in the SiO_2–Al_2O_3–Na_2O (Fig. 1a), SiO_2–Al_2O_3–MgO (Fig. 1b) and nepheline–forsterite–SiO_2 (Fig. 1c) composition systems, it is located in the crystallisation fields of cordierite ($Mg_2Al_4Si_5O_{18}$), nepheline ($Na_2Al_2Si_2O_8$) and spinel ($MgAl_2O_4$), respectively.

Fig. 2(a) depicts the DSC curves for powder (< 63 μm) and bulk RHA glass recorded at 50 °C/min. The figure shows that the devitrification process of RHA glass occurred through a surface crystallisation mechanism [33]. Thus, the most effective method for manufacturing glass-ceramic materials from RHA glass is by a sinter-crystallisation process, which involves the sintering and subsequent crystallisation of powdered glass. Therefore, the crystallisation study described below was performed on a glass sample that was ground and sieved to a particle size < 63 μm.

The first endothermic jump in the baseline at ≈ 600 °C corresponds to the glass transition temperature (Tg). After the Tg, two exothermic effects centred at ≈ 745 and

Table 1
Chemical composition (wt%) of rice husk ash and RHA glass.

Oxide	Rice husk ash	RHA glass
SiO_2	90.75	44.18
Al_2O_3	0.06	18.22
CaO	1.20	0.68
MgO	0.84	12.24
K_2O	1.56	1.86
Fe_2O_3	0.16	0.06
P_2O_5	3.62	0.48
Na_2O	—	17.06
B_2O_3	—	5.21
TiO_2	0.03	—
ZnO	0.01	—
SO_3	1.62	—
MnO	0.16	—

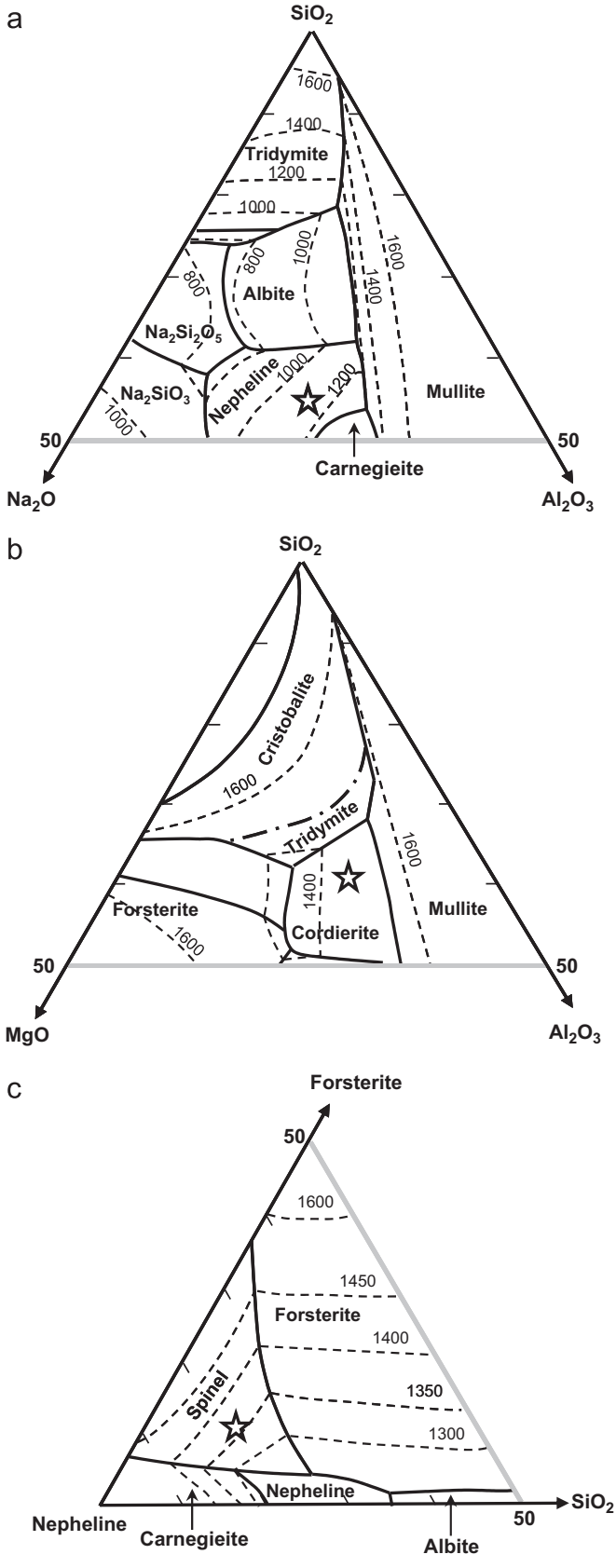

Fig. 1. Phase diagrams (wt%, T in °C) of the: (a) SiO_2–Al_2O_3–Na_2O system, (b) SiO_2–Al_2O_3–MgO system and (c) nepheline–forsterite–SiO_2 system indicating the RHA glass composition (☆).

900 °C indicate that the RHA glass is unstable on heating; thus, subsequent thermal treatment leads to a crystallisation process with the consequent formation of a glass-ceramic material. Finally, an endothermic reaction starting at ≈1100 °C indicates the formation of liquid phases. The XRD patterns collected on glass samples that were thermally treated for 60 min [33] indicate that the first exothermic effect (745 °C) corresponds to the crystallisation of nepheline ($Na_2O \cdot Al_2O_3 \cdot 2SiO_2$) from the parent glass, whereas the formation of forsterite ($2MgO \cdot SiO_2$) is responsible for the crystallisation effect centred at 900 °C.

Fig. 2(b) shows the plot of $\ln(\beta/T_p^2)$ versus $1/T_p$. A linear relationship was obtained for both crystallisation peaks, in accordance with the Kissinger equation (Eq. 1). The values of the activation energy (E) calculated from the slopes of these plots are 391 kJ/mol and 160 kJ/mol for the first and second crystallisation peaks, respectively. The value of E for the nepheline crystallisation (first DSC peak) is almost 150% greater than that corresponding to the formation of forsterite. This differentiation in the values of

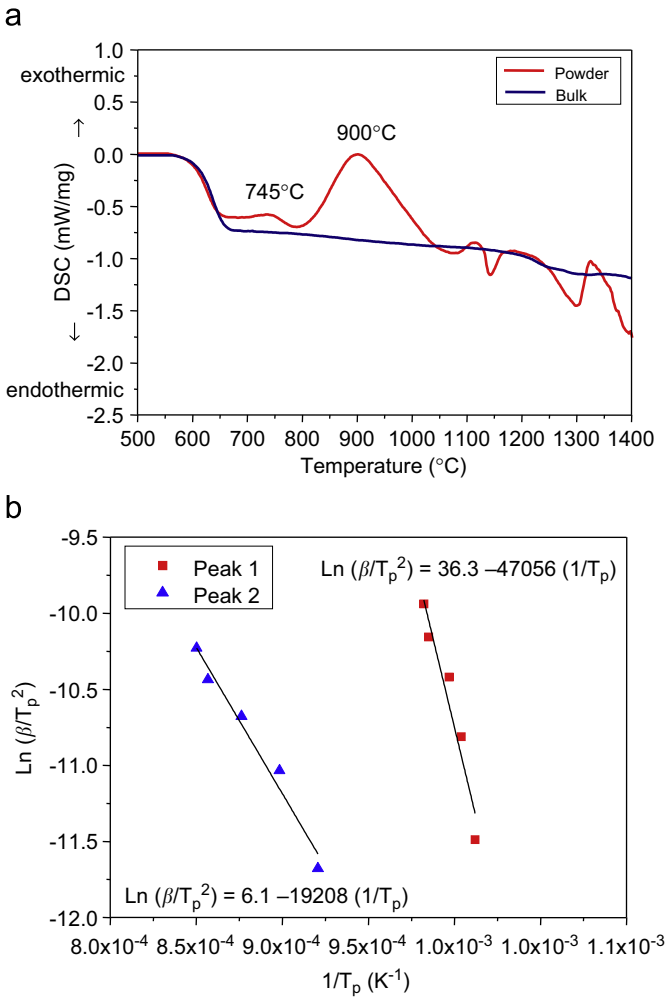

Fig. 2. (a) DSC curve (25–1450 °C, 50 °C/min) recorded on bulk and powder (< 63 μm) RHA glass, (b) Determination of the activation energy for crystallisation by the Kissinger equation (Peak 1 and Peak 2 correspond to the exotherms at 745 and 903 °C respectively).

the activation energy leads to differences in the degree of development of both crystalline phases after the crystallisation process, as explained below.

Fig. 3 presents the TTT (Time–Temperature–Transformation) diagrams for the RHA glass. The C-shaped curve, which is characteristic of nucleation and growth processes, shows the combinations of time and temperature needed for the onset of crystallisation. As usual in TTT curves, the lower heat treatment temperatures require longer times to initiate crystallisation; thus, the glass begins to devitrify after 40 min at 700 °C. As the temperature increases, the time required for the onset of crystallisation is reduced; consequently, the glass compacts are fully devitrified after 15 min at 750 °C. The fastest rates of crystallisation occurred at the highest temperatures employed (950 and 1000 °C), for which the onset time was only 2 min.

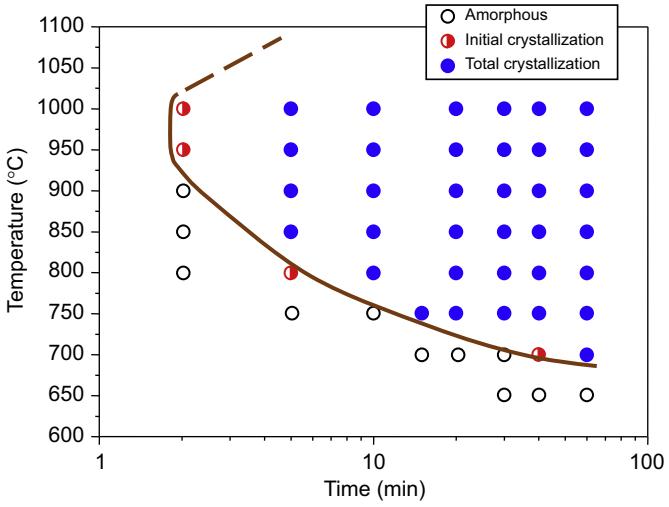

Fig. 3. TTT curve for RHA glass.

The XRD study conducted on all samples after heat treatment showed that devitrification of the RHA glass leads to a glass-ceramic material composed of nepheline ($Na_2O \cdot Al_2O_3 \cdot 2SiO_2$) and forsterite ($2MgO \cdot SiO_2$). Fig. 4 shows the intensity evolution (obtained from the collected data) of both crystalline phases as a function of temperature (700–1000 °C) and time (2–60 min). The diffraction lines at 2.46 and 3.40 Å for forsterite and nepheline, respectively, have been selected for the representation. It is important to note that nepheline and forsterite crystallise simultaneously during most of the heat treatments tested, although their respective crystallisation processes do not overlap in the DSC curve. This result is probably caused by the difference in the values of their respective activation energies, as determined by the Kissinger method. The onset of nepheline crystallisation is located at 700 °C in the DSC curve (Fig. 2a). The high activation energy associated with this process (391 kJ/mol) implies that a long holding time is required to promote the beginning of crystallisation; thus, nepheline is only detected by XRD after 40 min at 700 °C. This temperature is lower than that corresponding to the onset of forsterite crystallisation ($\approx$800 °C). However, because of its lower activation energy (160 kJ/mol), the holding time of 60 min is adequate to promote crystallisation in an isothermal process. Consequently, a minor quantity of forsterite is also detected after thermal treatment at 700 °C/60 min. In the treatment at 750 °C, the temperature is close to the maximum of the nepheline exothermic peak; consequently,

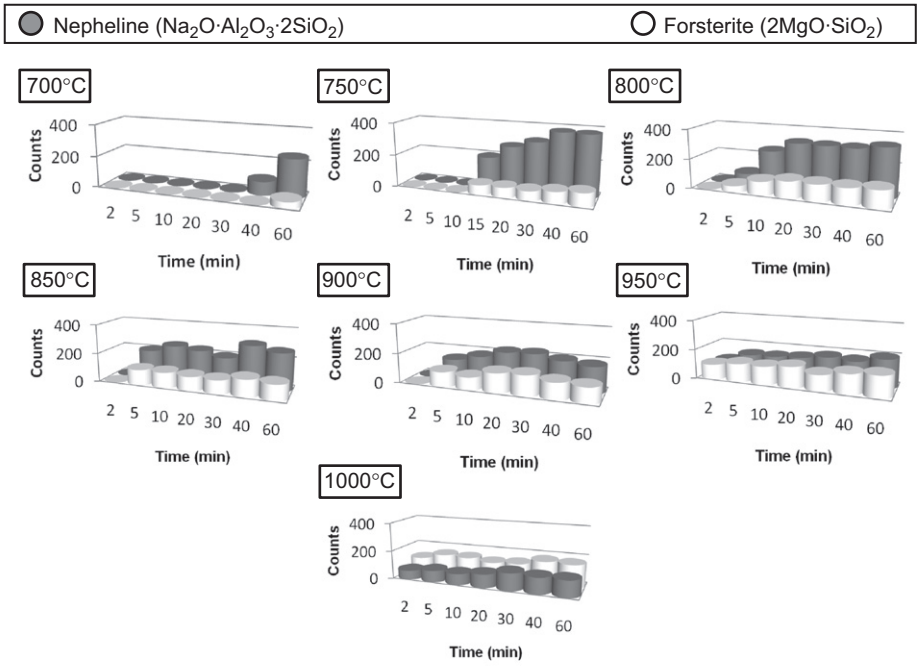

Fig. 4. Evolution of X-ray intensity for nepheline and forsterite phases as a function of temperature and time (T=700–1000 °C and t=2–60 min).

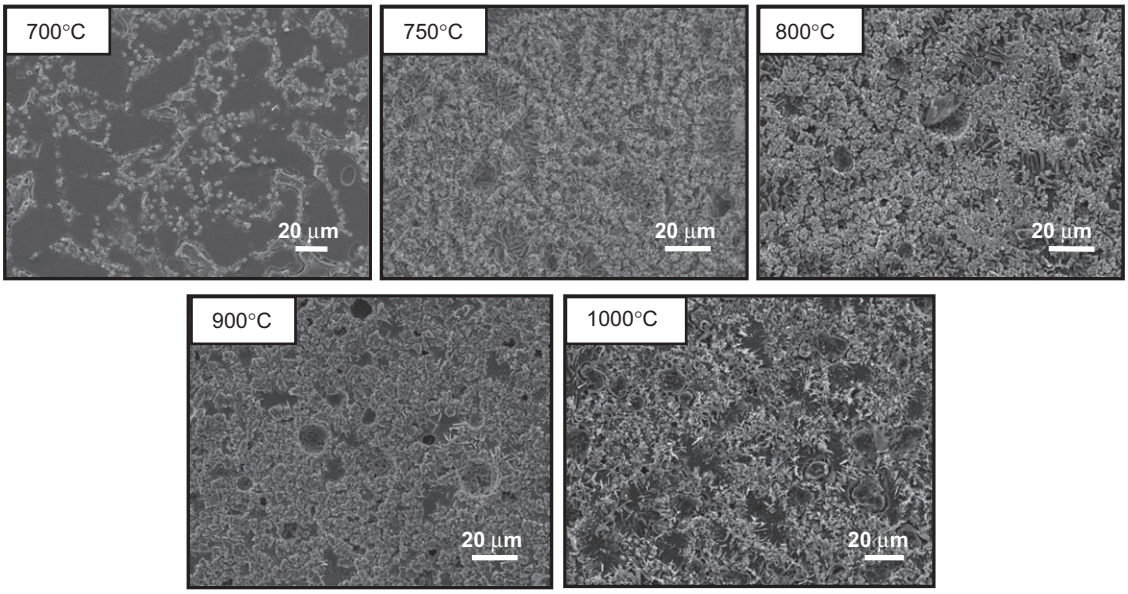

Fig. 5. Secondary electron images of RHA samples heat-treated at different temperatures (700–1000 °C) for 40 min.

the diffractograms taken on samples heated at 750 °C for 40 and 60 min reach the maximum X-ray intensity for the nepheline phase. As the temperature increases, the intensity of nepheline in the patterns decreases, while that of forsterite increases, reaching its maximum after the treatment at 1000 °C for 40 min.

Fig. 5 presents low magnification FESEM images of RHA glass samples heat-treated at various temperatures (700–1000 °C) for 40 min. The glass bodies exhibit good sintering behaviour and the fired samples show a homogeneous microstructure that is free of internal defects, such as delaminations or cracks. The crystallisation process takes places according to a mechanism of controlled surface crystallisation in which dense aggregates of crystals grow along the border line of the former glass grains. In the early stages of crystal growth (700 °C), the glass-ceramic exhibits a typical coast-and-island microstructure [1] that is characterised by crystal conglomerates that form a coast, while the glassy phase enclosed by the crystals has an island-like appearance. At 700 °C, a significant extent of open porosity is noticeable, which consists of interconnected elongated pores that produce channels along the glass-crystal interface. When crystallisation proceeds, the crystals grow inside the remaining glass, the phase boundaries disappear and the coasts and islands are indistinguishable. The glass-ceramic produced at 750 °C exhibits a high degree of crystallisation with a microstructure that consists of a significant concentration of crystals together with a residual glassy phase constrained to the centre of the larger former glass particles. Open porosity is still perceptible, although the channels observed at 700 °C are no longer detected. As the temperature increases, the open porosity is reduced, but close porosity consisting of rounded pores increases simultaneously. Furthermore, temperatures above 900 °C cause an increase in the glassy phase, which is likely caused by the partial dissolution of the nepheline phase developed at lower temperatures (Fig. 4).

Figs. 6–11 show FESEM images and XRD patterns of the glass-ceramics produced at the temperature–time conditions indicated in Fig. 5. Table 2 collects the EDX analyses of the glassy and crystalline phases observed in the glass-ceramic materials after the different thermal treatments. The XRD diffractogram of the material produced after thermal treatment at 700 °C/40 min (Fig. 6a) shows that the crystallisation process begins with the precipitation of nepheline, although the amount of the glassy phase in the glass-ceramic remains significant, as indicated by the intensity of the amorphous halo. Fig. 6(b) shows that nepheline crystals (*N*) outline the coast in the coast-and-island microstructure described above. At 700 °C, the crystalline and glassy phases exhibit a similar chemical composition (Table 2), the main difference between them is their MgO content, which preferentially remains in the residual glass. It should be noted that the SiO_2/Al_2O_3 ratio in the nepheline crystals is 2.36, which is twice the ratio corresponding to the stoichiometric nepheline composition with $SiO_2/Al_2O_3 = 1.18$ [47]. The usual morphology of nepheline crystals is stout prisms [48]. Nevertheless, the detailed observation of the microstructure developed at 700 °C (Fig. 6c) shows pseudo-hexagonal thin plates of nepheline growing in a uniaxial arrangement, producing aggregates with an unusual pinecone-like structure. Hexagonal tabular plates are the characteristic morphology of tridymite (SiO_2). Hence, both the high silica content in the EDS analyses and the tabular morphology of the crystals suggest that nepheline development proceeds through a stuffed derivative structure of silica [49,50]. Accordingly, the structure of nepheline ($(Na,K)AlSiO_4$) can be derived from the structure of high

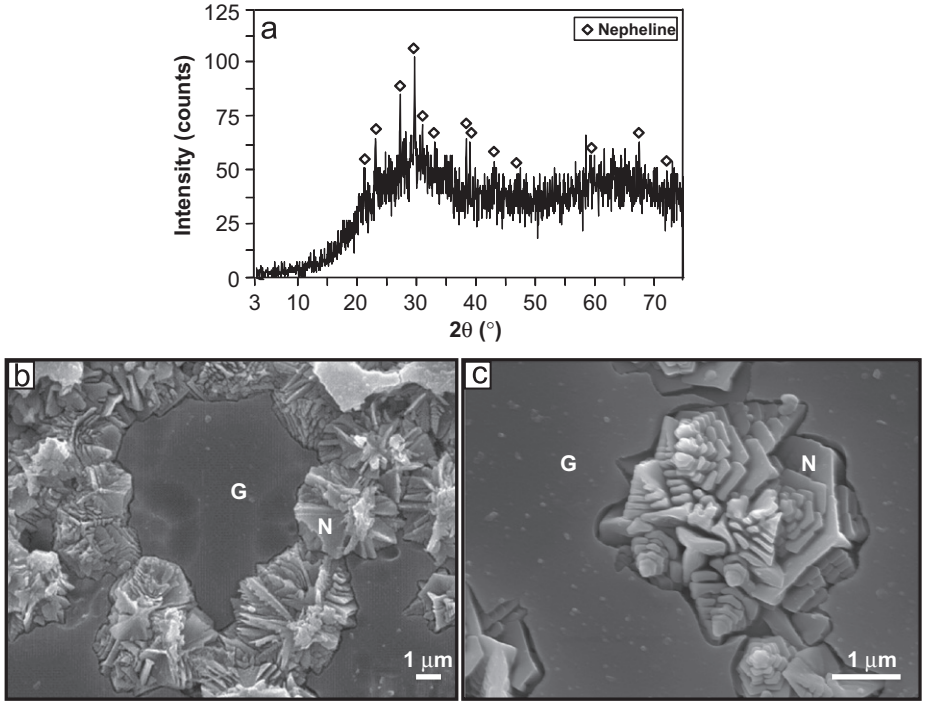

Fig. 6. XRD patterns (a) and secondary electron images (b) 6000x and (c) 18000x of samples heat-treated at 700 °C for 40 min (G = glassy phase, N = nepheline).

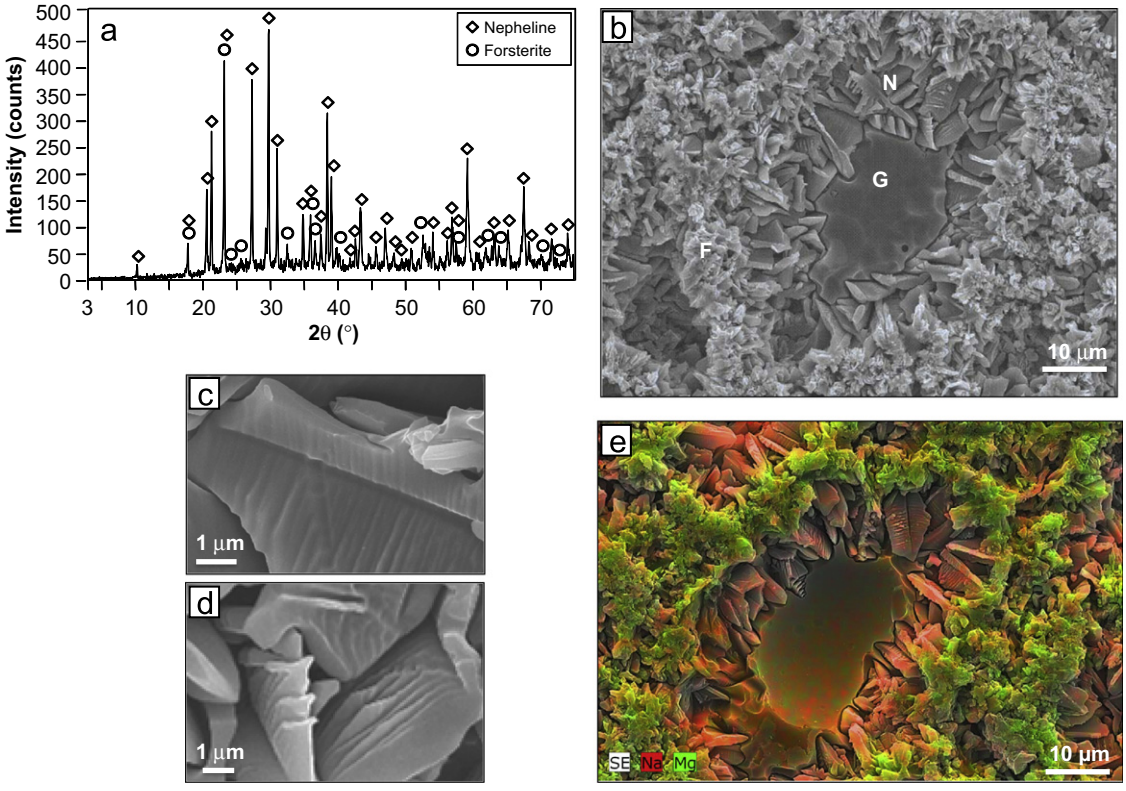

Fig. 7. XRD pattern (a), secondary electron image (b), detail of the microstructure of nepheline and forsterite (c,d) and secondary electron image together with the elemental mapping of Na (red colour) and Mg (green colour) (e) of the sample heat-treated at 750 °C for 40 min (G = glassy phase, N = nepheline, F = forsterite). (For interpretation of the references to colour in this figure legend, the reader is referred to the web version of this article.)

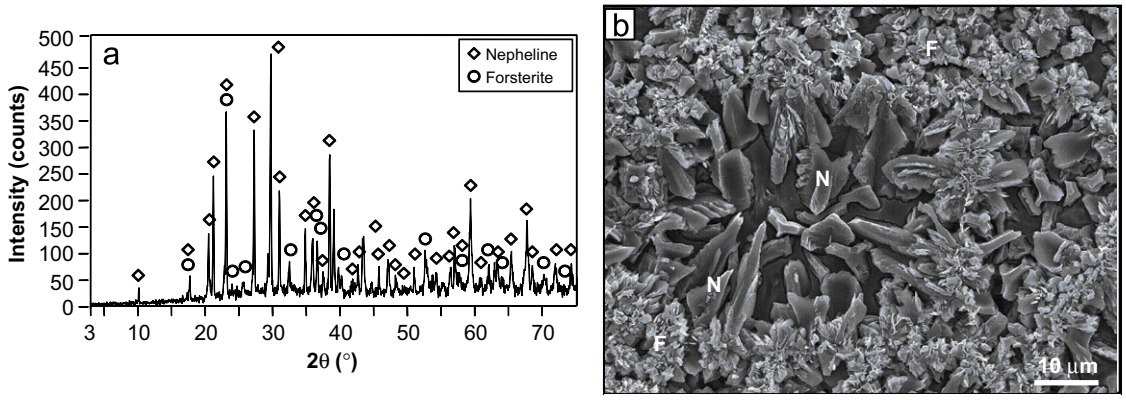

Fig. 8. XRD pattern (a) and secondary electron image (b) of the sample heat-treated at 800 °C for 40 min (N=nepheline, F=forsterite).

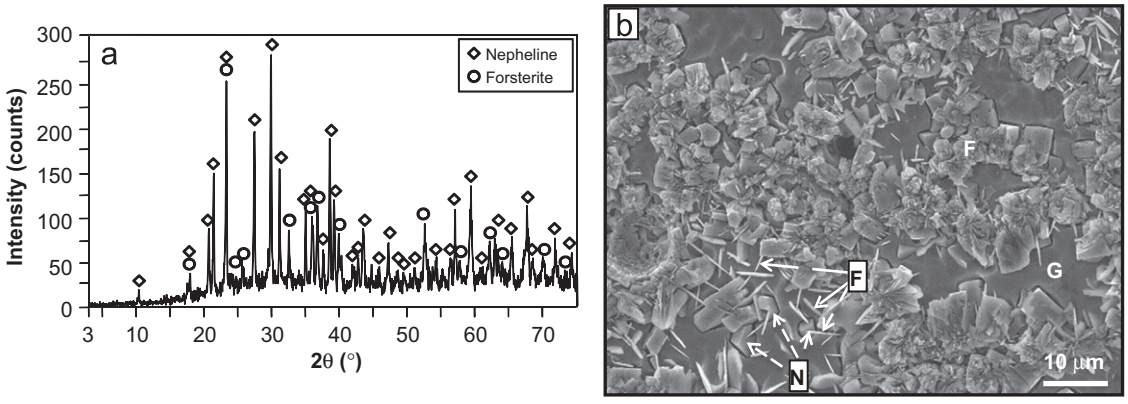

Fig. 9. XRD pattern (a) and secondary electron image (b) of the sample heat-treated at 900 °C for 40 min (G=glassy phase, N=nepheline, F=forsterite).

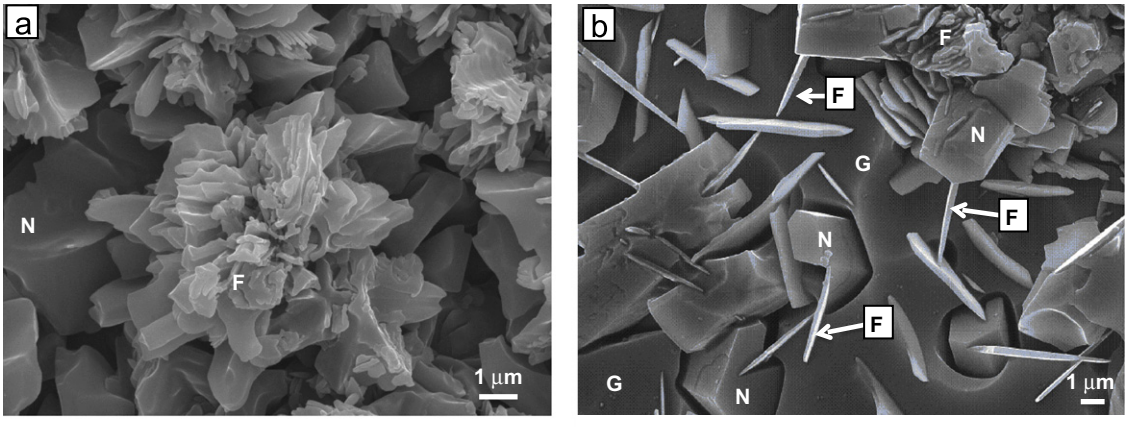

Fig. 10. Secondary electron images of the samples heat-treated at 800 °C (a) and 900 °C (b) for 40 min (G=glassy phase, N=nepheline, F=forsterite).

tridymite by substituting NaAl for Si to form structures with planar wurtzite-type nets [51]. The thermal treatment at 750 °C leads to an increase in the crystallisation degree, as indicated by the attenuation of the amorphous halo observed in the diffraction pattern (Fig. 7a). The nepheline phase remains the predominant crystalline phase, and its diffraction intensity increases significantly compared to the diffractogram at lower temperature, although low intensity diffraction peaks corresponding to forsterite are also detected. FESEM observations (Fig. 7b) allow both the residual glass and crystalline phases to be distinguished, and the latter phase is composed of crystals with two

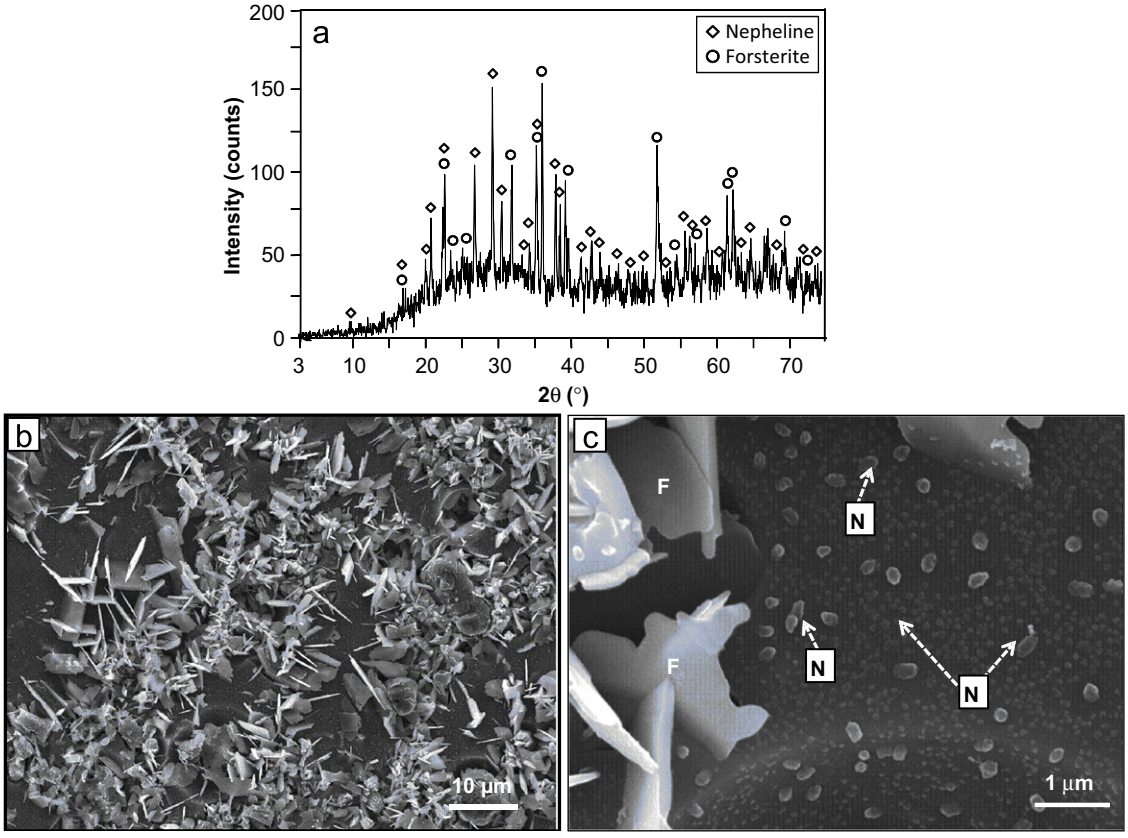

Fig. 11. XRD pattern (a) and secondary electron images (b) 1500x, (c) 16000x of the sample heat-treated at 1000 °C for 40 min (N=nepheline, F=forsterite).

Table 2
EDS analyses (wt%) of the glassy and crystalline phases of RHA glass heat treated at different temperatures.

Thermal treatment	Phase	SiO_2	Al_2O_3	Na_2O	K_2O	MgO	SiO_2/MgO
700 °C/ 40 min	Glassy phase	52.99	18.86	15.65	1.10	11.40	4.65
	Nepheline	54.48	23.10	15.80	0.90	5.73	
750 °C/ 40 min	Glassy phase	56.08	17.70	14.46	1.65	10.10	5.55
	Nepheline	54.35	24.42	17.04	1.22	2.98	
	Forsterite	51.10	16.61	9.88	1.09	21.32	2.40
800 °C/ 40 min	Glassy phase	56.11	13.34	18.02	1.20	11.34	4.95
	Nepheline	53.06	24.55	15.59	1.38	5.43	
	Forsterite	54.35	14.24	8.35	0.48	27.84	1.95
900 °C/ 40 min	Glassy phase	57.58	16.88	16.03	1.03	8.49	6.78
	Nepheline	53.02	25.97	16.04	1.19	3.77	
	Forsterite	50.32	12.74	7.99	0.76	28.18	1.78
1000 °C/ 40 min	Glassy phase	57.16	19.54	14.01	1.31	8.20	6.97
	Nepheline	52.27	22.85	15.41	0.81	8.67	
	Forsterite	48.28	10.12	17.04	0.72	33.84	1.42

different morphologies. The differences in the EDS analyses collected from these crystals (Table 2), especially in the magnesium content, make it possible to associate each crystal morphology with a crystalline phase identified by XRD. Thus, the elongated and flattened bladed crystals correspond to nepheline, which grows surrounding or mingling with the residual glassy phase. Frequently, nepheline crystals exhibit a lamellar twinned microstructure, as shown in Fig. 7(c). The pinecone aggregates of nepheline crystals observed at 700 °C are undetectable at higher

temperatures. In the case of the forsterite phase (*F*), crystals develop as thin flakes or plates arranged in a flattened radial habit around a central point, giving rise to rose-shaped clusters of crystals. The forsterite plates always grow in association with nepheline crystals, and it is possible to observe the development of forsterite flakes embedded into nepheline crystals, as shown in Fig. 7(d). Fig. 7(e) shows a FESEM image together with the elemental mapping of Na (red colour) and Mg (green colour). The nepheline and forsterite phases are clearly identified by colour dissimilarities caused by different concentrations of these ions in each of the crystalline phases.

The increase of the thermal treatment temperature to 800 °C leads to negligible changes in both the mineralogy and microstructure of the resulting glass-ceramics (Fig. 8). The XRD pattern depicts a similar distribution of the amorphous and crystalline phases, and the morphology and arrangement of the crystalline phases is comparable to that observed at 750 °C. The most significant microstructural and mineralogical changes are observed after the thermal treatment at 900 °C (Fig. 9). The intensity of the nepheline peaks in the XRD diffractogram (Fig. 9a) decrease considerably, and the amorphous halo intensifies simultaneously. This result indicates the partial dissolution of the nepheline crystals developed at lower temperatures, thus increasing the amount of the glassy phase, as shown in the FESEM micrograph (Fig. 9b). The treatment at 900 °C also leads to a new change in the morphology of the nepheline crystals, which appear as hexagonal prisms (the hexagonal morphology is more clearly shown in Fig. 10b). The proportion of the forsterite phase in the glass-ceramic is nearly invariable, as indicated by the comparable intensity of the forsterite peaks in the diffractograms at 800 °C and 900 °C. Nevertheless, some microstructural variations with respect to the forsterite crystals developed at 800 °C are observed. Fig. 10 shows higher magnification observations of the forsterite crystals in the glass-ceramics produced at both 800 °C and 900 °C. At 800 °C, most of the forsterite crystals are linked to nepheline crystals, producing the rose-shaped aggregates (Fig. 10a) described above. These aggregates develop in minor amounts in the materials obtained at 900 °C (Fig. 10b) and the partial dissolution of nepheline causes most of the forsterite flakes that appeared at 800 °C embedded into nepheline crystals to become isolated and to be included in the glassy phase.

The dissolution of the nepheline crystals and the subsequent increase in the glassy phase is even more remarkable in the glass-ceramics produced at 1000 °C, as can be observed in both the XRD diffractogram (Fig. 11a) and the FESEM observation (Fig. 11b). The amorphous halo is significantly enhanced by the greater dissolution of the nepheline phase, and the intensity of the diffraction peaks associated to forsterite increases. Forsterite flakes appear randomly oriented and interlocking with each other, leading to a house-of-cards microstructure. The glassy phase, which was observed with a homogeneous morphology at lower temperatures, exhibits a characteristic texture at 1000 °C. A higher magnification FESEM micrograph (Fig. 11c) allows for observation of the occurrence of numerous small granules, which correspond to the remains of the nepheline crystals that undergo dissolution by the glassy phase.

The chemical composition of the different crystalline phases developed on heating (Table 2) generally exhibit insignificant compositional differences with increasing temperature. As expected, the magnesium ions are mainly retained in the forsterite crystals and the aluminium ions are mainly retained in the glassy phase after crystallisation. The sodium ions assume similar proportions in both the glassy phase and the nepheline crystals. Although the silicon is located in different phases, its content in the glassy phase is slightly higher. The only significant difference found is the evolution of the SiO_2/MgO ratio in the glass phase and in forsterite crystals developed at different temperatures. Thus, as the forsterite content increases with increasing crystallisation temperature, the percentage of magnesium in the forsterite crystals increases with the consequent decrease in the SiO_2/MgO ratio, while this ratio increases in the glassy phase.

For a previous knowledge of technological features of these materials, the glass-ceramic obtained after thermal treatment at 900 °C/40 min has been tested in order to determine its water absorption (0.41%), bending strength (39 N/mm^2) and Mohs hardness (8) values. With these properties, the developed glass-ceramic are within BIa group (dry pressed ceramic tiles with water absorption E $< 0.5\%$) of the standard ISO 13006 and are suitable for floor pavement and wall covering in both indoor and outdoor applications. Currently, a study is being conducted to determine the technological properties of the forsterite–nepheline glass-ceramics produced at different thermal treatments to assess their possible fields of application, including their use as ceramic tiles.

4. Conclusions

The results obtained in this investigation show the feasibility of the production of a wide variety of forsterite–nepheline glass-ceramics with different microstructure by a sinter-crystallisation process from a SiO_2–Al_2O_3–MgO–Na_2O base glass formulated with rice husk ash (RHA) as a silica source.

The DTA curve shows two exothermic effects centred at 745 and 900 °C, which correspond to nepheline ($Na_2O \cdot Al_2O_3 \cdot 2SiO_2$) and forsterite ($2MgO \cdot SiO_2$) devitrification, respectively. The activation energies associated with these crystallisation processes are 391 kJ/mol for nepheline formation and 160 kJ/mol for forsterite formation.

Glass begins to crystallise after 40 min at 700 °C and that the glass compacts are fully devitrified after 15 min at 750 °C. The fastest rate of crystallisation occurs at 950 °C, at which the onset time for crystallisation is only 2 min. The main crystalline phases in the glass-ceramic materials

are nepheline in the temperature interval 700–950 °C and forsterite at temperatures above 950 °C.

In the early stages of crystal growth (700 °C), the glass-ceramic exhibits a typical coast-and-island microstructure and nepheline appears as pseudo-hexagonal thin plates growing in a uniaxial arrangement, produce aggregates with a pinecone-like structure. At higher temperatures, nepheline develops as elongated and flattened bladed crystals, which frequently exhibit a lamellar twinned microstructure. In the case of the forsterite phase, crystals develop as thin flakes or plates arranged in a flattened radial habit around a central point, giving rise to rose-shaped clusters of crystals. The most significant microstructural and mineralogical changes are observed after the thermal treatment at 900 °C. Nepheline crystallises as hexagonal prisms and forsterite flakes appear randomly oriented and interlocking, leading to a house-of-cards microstructure.

Acknowledgements

Dr. M.I. Martín expresses her gratitude to the Spanish National Research Council (CSIC) for her contract through the JAE Programme (JAEDoc-08–00032), co-financed by the European Social Fund. The authors thank Mrs. P. Díaz for her technical assistance and IRICA from the University of Castilla-La Mancha (Spain) for experimental assistance with XRD.

References

[1] W. Hölland, G. Beall, Glass-ceramic technology, The American Ceramic Society (2002) Ohio.
[2] E. Willhauk, R. Harikantha, Low Thermal Expansion Glass-Ceramics, 2nd ed., Springer Verlag, Heidelberg, 2005.
[3] N. Kanchanarat, S. Bandyopadhyay-Ghosh, I.M. Reaney, I.M. Brook, P.V. Hatton, Microstructure and mechanical properties of fluorcanasite glass-ceramics for biomedical applications, Journal of Materials Science 43 (2008) 759–765.
[4] R. Casasola, J.Ma. Rincón, M. Romero, Glass-ceramic glazes for ceramic tiles—a review, Journal of Materials Science 47 (2012) 553–582.
[5] E.I. Suzdal'tsev, D.V. Kharitonov, A.A. Anashkina, Analysis of existing radioparent refractory materials, composites and technology for creating high-speed rocket radomes. Part 4. Ceramic technology for producing glass ceramic radomes. Advantages and disadvantages. Prospects for modernization, Refractories and Industrial Ceramics 51 (2011) 349–357.
[6] A.A. Shapiro, N. Kubota, Yu K, M.L. Mecartney, Stress testing of a recrystallizing $CaO–B_2O_3–SiO_2$ glass-ceramic with Ag electrodes for high frequency electronic packaging, Journal of Electronic Materials 30 (2011) 386–390.
[7] J.Ma. Rincon, Principles of nucleation and controlled crystallization of glasses, Polymer-Plastics Technology Engineering 31 (1992) 309–357.
[8] S.R. Teixeira, M. Romero, J Ma., Rincón, crystallization of $SiO_2–CaO–Na_2O$ glass using sugarcane bagasse ash as silica source, Journal of American Ceramics Society 93 (2010) 450–455.
[9] W.A. Deer, R.A. Howie, J. Zussman, An Introduction to the Rock-Forming Minerals, 2nd ed., Pearson, London, 1992.
[10] L. Lin, M. Yin, C. Shi, W. Zhang, Luminiscence properties of a new red long-lasting phosphor $Mg_2SiO_4:Dy^{3+}$, Mn^2, Journal of Alloys and Compounds 455 (2008) 327–330.
[11] S. Ni, L. Chou, J. Chang, Preparation and characterization of forsterite (Mg_2SiO_4) bioceramics, Ceramics International 33 (2007) 83–88.
[12] H.E. Swanson, E. Targe, National Bureau of Standards (US) Circular 359 (1953) 83–86.
[13] F. Tavangarian, R. Emadi, Mechanical activation assisted synthesis of pure nanocrystalline forsterite powder, Journal of Alloys and Compounds 485 (2009) 648–652.
[14] M.H.E. Martin, C.K. Ober, C.R. Hubbard, W.D. Porter, O.B. Cavin, Poly(methacrylate) precursors to forsterite, Journal of the American Ceramic Society 75 (1992) 1831–1838.
[15] S. Ni, L. Chou, J. Chang, Preparation and characterization of forsterite (Mg_2SiO_4) bioceramics, Journal of Ceramics International 33 (2007) 83–88.
[16] E. Mustafa, N. Khalil, A. Gamal, Sintering and microstructure of spinel-forsterite bodies, Ceramics International 28 (2002) 663–667.
[17] T.S. Sasikala, M-N. Suma, P. Mohanan, C. Pavithran, M.T. Sebastian, Forsterite-based ceramic-glass composites for substrate applications in microwave and millimeter wave communications, Journal of Alloys and Compounds 461 (2008) 555–559.
[18] P. Amista, M. Cesari, A. Montenero, G. Gnappi, L. Lan, Crystallization behaviour in the system $MgO–Al_2O_3–SiO_2$, Journal of Non-Crystalline Solids 192&193 (1995) 529–533.
[19] Y. Hu, H.T. Tsai, Compositional effect on the crystallization of the cordierite-type glasses, Journal of Materials Science 36 (2001) 123–129.
[20] S.R. Lacerda, J.M. Oliveira, R.N. Correia, M.H.V. Fernandes, TiO-induced phase separation and crystallization in $SiO_2–3Ca \cdot P_2O_5–MgO$ glass, Journal of Non-Crystalline Solids 221 (1997) 55–60.
[21] G. Khater, Crystallizing phases from multi-component silicate glasses in the system $K_2O–CaO–MgO–Al_2O_3–SiO_2$, Ceramics International 27 (2011) 661–668.
[22] Y. Demirci, E. Günay, Crystallization behavior and properties of cordierite glass-ceramics with added boron oxide, Journal of Ceramic Processing Research 12 (2001) 352–356.
[23] J.F. Mac Dowell, Microwave heating of nepheline glass-ceramics, Journal of the American Ceramic Society 58 (1975) 258–259.
[24] M.C. Wang, N.C. Wu, M.H. Hon, Preparation of nepheline glass-ceramics and their Application as dental porcelain, Materials Chemical Physics 37 (1994) 370–375.
[25] E.M.A. Hamzawy, E.M. El-Meliegy, Preparation of nepheline glass-ceramics for dental applications, Materials Chemistry and Physics 112 (2008) 432–435.
[26] E.M.A. Hamzawy, E.M. El-Meliegy, Crystallization in the $Na_2O–CaO–Al_2O_3–SiO_2–(LiF)$ glass compositions, Ceramics International 33 (2007) 227–231.
[27] E.M.A. Hamzawy, C. Leonelli, Crystallization, microstructure and expansitivity of apodumene–nepheline glasses, Glass Science and Technology 77 (2004) 289–294.
[28] M. Romero, M. Kovacova, J.Ma. Rincón, Effect of particle size on kinetics crystallization of an iron-rich glass, Journal of Materials Science 43 (2008) 4135–4142.
[29] M.S. Hernandez-Crespo, M. Romero, J.Ma. Rincon, Nucleation and crystal growth of glasses produced by a generic plasma arc-process, Journal of the European Ceramic Society 26 (2006) 1679–1685.
[30] M. Romero, M.S. Hernandez-Crespo, J.Ma. Rincon, Leaching behaviour of a glassy slag and derived glass ceramics from arc plasma vitrification of hospital wastes, Advances in Applied Ceramics 108 (2009) 67–71.
[31] N. Kanchanarat, S. Bandyopadhyay-Ghosh, I.M. Reaney, Microstructure and mechanical properties of fluorcanasite glass-ceramics for biomedical applications, Journal of Materials Science 43 (2008) 759–765.
[32] F.A. López, M.I Martín, F.J. Alguacil, J.Ma. Rincón, TA. Centeno, Thermolysis of fibreglass polyester composite and reutilisation of the glass fibre residue to obtain a glass-ceramic material, Journal of Analytical and Applied Pyrolysis 93 (2012) 104–112.

[33] M.I. Martín, M. Romero, J.Ma. Rincón, F. Andreola, L. Barbieri, F. Bondioli, I. Lancellotti, Materiales vitrocerámicos del sistema $MgO–Al_2O_3–SiO_2$ a partir de ceniza de cáscara de arroz, Boletin de la Sociedad Espanola de Ceramica y Vidrio 50 (2011) 201–206.
[34] F. Bondioli, F. Andreola, L. Barbieri, T. Manfredini, A.M. Ferrari, Effect of rice husk ash (RHA) in the synthesis of $(Pr,Zr)SiO_4$ ceramic pigment, Journal of the European Ceramic Society 27 (2007) 3483–3488.
[35] F. Bondioli, L. Barbieri, A.M. Ferrari, T. Manfredini, Characterization of rice husk ash and its recycling as quartz substitute for the production of ceramic glazes, Journal of the American Ceramic Society 93 (2010) 121–126.
[36] T. Luangvaranunt, C. Dhadsanadhep, J. Umeda, E. Nisaratanaporn, K. Kondoh, Aluminum-4 mass% copper/alumina composites produced from aluminum copper and rice husk ash silica powders by powder forging, Materials Transactions 51 (2010) 756–761.
[37] G.C. Cordeiro, R.D. Toledo, E.D.R. Fairbairn, Use of ultrafine rice husk ash with high-carbon content as pozzolan in high performance concrete, Materials and Structures 42 (2009) 983–992.
[38] B.K. Ngun, H. Mohamad, E. Sakai, Z.A. Ahmad, Effect of rice husk ash and silica fume in ternary system on the properties of blended cement paste and concrete, Journal of Ceramic Processing Research 11 (2010) 311–315.
[39] C.S. Prasad, K.N. Maiti, R. Venugopal, Effect of substitution of quartz by rice husk ash and silica fume on the properties of whiteware compositions, Ceramics International 29 (2003) 907–914.
[40] F. Andreola, L. Barbieri, F. Bondioli, Agricultural waste in the synthesis of coral ceramic pigment, Dyes and Pigments 94 (2012) 207–211.
[41] D. Wattanasiriwech, N. Polpuak, P. Danthaisong, S. Wattanasiriwech, Use of rice husk ash for quartz substitution in stoneware glazes, Journal of Scientific and Industrial Research 67 (2008) 455–460.
[42] F. Andreola, L. Barbieri, F. Bondioli, A.M. Ferrari, T. Manfredini, Valorization of rice husk ash as secondary raw material in the ceramic industry, in: Proceedings of the 10th International Conference of European Ceramic Society (ECERS), Baden-Baden, Germany 2007, pp. 1794–1798.
[43] J.P. Nayak, S. Kumar, J. Bera, Sol–gel synthesis of bioglass-ceramics using rice husk ash as a source for silica and its characterization, Journal of Non-Crystalline Solids 356 (2010) 1447–1451.
[44] M.K. Naskar, M. Chatteljee, A novel process for the synthesis of lithium aluminum silicate powders from rice husk ash and other water-based precursor materials, Materials Letters 59 (2005) 998–1003.
[45] M.K. Naskar, M. Chatterjee, A novel process for the synthesis of cordierite ($Mg_2Al_4Si_5O_{18}$) powders from rice husk ash and other sources of silica and their comparative study, Journal of the European Ceramic Society 24 (2004) 3499–3508.
[46] H. Kissinger, Reaction kinetics in differential thermal Analysis, Analytical Chemistry 29 (1957) 1702–1706.
[47] 〈http://www.webmineral.com/data/Nepheline.shtml〉.
[48] 〈http://www.mindat.org/min-2880.html〉.
[49] M.J. Buerger, Derivative crystal structures, Journal of Chemical Physics 15 (1947) 1–16.
[50] R.N. Abbott, $KAlSiO_4$ Stuffed derivatives of tridymite: phase relationships, American Mineralogist 69 (1984) 449–457.
[51] R.B. Heimann, Classic and Advanced Ceramics: From Fundamentals to Applications, John Wiley & Sons, Weinheim, 2010.